remote sensing

MDPI

Article

Interannual Variability and Trends in Extreme Precipitation in Dronning Maud Land, East Antarctica

Lejiang Yu [1,*], Shiyuan Zhong [2], Svetlana Jagovkina [3], Cuijuan Sui [4] and Bo Sun [1]

[1] State Oceanic Administration Key Laboratory for Polar Science, Polar Research Institute of China, No. 451, Jinqiao Road, Pudong New District, Shanghai 200136, China; sunbo@pric.org.cn
[2] Department of Geography, Environment and Spatial Sciences, Michigan State University, East Lansing, MI 48824, USA; zhongs@msu.edu
[3] Arctic and Antarctic Research Institute, Saint Petersburg 199397, Russia; svja05@yandex.ru
[4] National Marine Environmental Forecasting Center, Beijing 100081, China; suicj@nmefc.cn
* Correspondence: yulejiang@sina.com.cn or yulejiang@pric.org.cn

Abstract: This study examines the trends and interannual variability of extreme precipitation in Antarctica, using six decades (1963–2023) of daily precipitation data from Russia's Novolazarevskaya Station in East Antarctica. The results reveal declining trends in both the annual number of extreme precipitation days and the total amount of extreme precipitation, as well as a decreasing ratio of extreme to total annual precipitation. These trends are linked to changes in northward water vapor flux and enhanced downward atmospheric motion. The synoptic pattern driving extreme precipitation events is characterized by a dipole of negative and positive height anomalies to the west and east of the station, respectively, which directs southward water vapor flux into the region. Interannual variability in extreme precipitation days shows a significant correlation with the Niño 3.4 index during the austral winter semester (May–October). This relationship, weak before 1992, strengthened significantly afterward due to shifting wave patterns induced by tropical Pacific sea surface temperature anomalies. These findings shed light on how large-scale atmospheric circulation and tropical-extratropical teleconnections shape Antarctic precipitation patterns, with potential implications for ice sheet stability and regional climate variability.

Keywords: Antarctic climate; climate change; extreme precipitation; climate variability; ENSO; teleconnection

Academic Editor: Yuriy Kuleshov

Received: 28 October 2024
Revised: 24 December 2024
Accepted: 15 January 2025
Published: 17 January 2025

Citation: Yu, L.; Zhong, S.; Jagovkina, S.; Sui, C.; Sun, B. Interannual Variability and Trends in Extreme Precipitation in Dronning Maud Land, East Antarctica. *Remote Sens.* **2025**, *17*, 324. https://doi.org/10.3390/rs17020324

1. Introduction

Precipitation is a critical component of the Antarctic ice sheet surface mass balance [1], and its changes and variability directly impact the ice sheet's mass, contributing to global sea level change [2,3]. Understanding the amount, sources, and spatiotemporal patterns of Antarctic precipitation is essential for the accurate interpretation of ice core data and the reconstruction of paleoclimatic signals [4,5]. Recent studies indicate that 40% of the annual precipitation and 70% of its interannual variability arise from just 10% of the largest daily precipitation events [6]. Notably, extreme precipitation events during the austral winters of 2019 and 2020 reduced mass loss by 60 $\pm$ 16 Gt yr^{-1}, contributing negatively to the overall loss of 107 $\pm$ 15 Gt yr^{-1} [3]. These events also introduce significant biases in annual air temperature interpretations from ice core data [5,7,8]. Therefore, it is crucial to investigate the trends and variability of extreme precipitation in Antarctica, as well as the factors that influence them.

Previous studies have examined the synoptic regimes associated with Antarctic extreme precipitation events. Several case studies found that these events often coincide

with the presence of atmospheric rivers (ARs) over the Southern Ocean [9–13]. Extreme precipitation in Antarctica is also frequently linked to cyclones and fronts over the Southern Ocean [14,15], which interact with the complex terrain of the continent, further intensifying precipitation amounts [16,17]. Atmospheric wavetrains over the Southern Ocean can lead to the formation of atmospheric blockings [18–20], which promote the occurrence of extreme precipitation events [20–22]. Case studies of extreme precipitation events at various stations have also identified atmospheric circulation and water vapor flux anomalies accompanying these events. For instance, Birnbaum et al. [23] revealed three synoptic conditions that triggered extreme precipitation at Kohnen Station, including occluding fronts of eastward-moving low-pressure systems, secondary lows, and large-scale lifting processes. Similarly, Yu et al. [24] and Yang et al. [25] analyzed synoptic circulation and water vapor transport anomalies at several stations in East Antarctica, including Progress Station in the Prydz Bay region, Casey Station in the Windmill Islands along the coast of Wilkes Land, and Vostok Station at the center of the East Antarctic Ice Sheet.

In addition to synoptic processes, several climate modes influence the interannual variability of Antarctic extreme precipitation occurrences. Schlosser et al. [26], using two years of data, noted that more (fewer) extreme precipitation events at Dome C in 2009 (2010) were linked to greater (lesser) water vapor transport, which corresponded to the negative (positive) phase of the Southern Annular Mode (SAM) and the positive (negative) phase of the Zonal Wavenumber 3 (ZW3) pattern. Marshall et al. [27], based on simple correlation analysis, suggested that at Byrd Station in West Antarctica, the number of days with extreme precipitation is associated with the positive phases of SAM and the Southern Baroclinic Annular mode (BAM) and the positive (negative) phases of the Pacific South American 1 (PSA1) and 2 (PSA2) modes. At Law Dome, more extreme precipitation occurrences were linked to the positive BAM and the negative SAM. Turner et al. [6] found that during austral winter and spring, ENSO resulted in more extreme precipitation over the Ross Sea and Marie Byrd Land, but less over the Bellingshausen Sea. Additionally, the positive SAM phase during austral spring, autumn, and winter led to more extreme precipitation over the Antarctic Peninsula and less over the Ross Ice Shelf. Furthermore, Antarctic sea ice loss can increase the number of extreme precipitation days, with ocean dynamics and ocean-atmosphere interactions playing a key role in the processes [28].

Previous studies have also investigated trends in the frequency and amount of Antarctic extreme precipitation. Turner et al. [29] linked an increasing trend in precipitation days at Faraday/Vernadsky Station on the western Antarctic Peninsula to a shift toward the positive phase of SAM. Yu et al. [24] attributed the positive trend in extreme precipitation days and amounts at Progress Station to thermodynamic processes, particularly increased water vapor content north of the station.

Dronning Maud Land (DML), located in East Antarctica (20°W–45°E), is characterized by steep topography [30], which strongly influences the spatial distribution of snow [31]. Extreme precipitation is common in DML, particularly along its coast, where it accounts for more than 50% of the annual precipitation [6]. Several studies have examined extreme precipitation in DML [9,18,21,23,32–35]. Turner et al. [6] showed that between 1979 and 2016, extreme precipitation amounts exhibited an increasing trend in southern DML, while a decreasing trend was observed inland of the coast across 100–120°E. For the period 1979–2018, much of the DML experienced an increase in extreme precipitation days, attributed to higher moisture availability and stronger poleward meridional winds in the Atlantic sector of the Southern Ocean [35].

Most of these studies have relied on reanalysis data and regional models, which are not well-suited for accurately capturing extreme precipitation. In contrast, studies based on in situ observations have often used relatively short records (fewer than 40 years),

limiting their ability to fully capture the relationship between extreme precipitation and low-frequency climate modes. Among previous studies, only Turner et al. [6] examined the relationship between the Antarctic annual extreme precipitation amount and SAM and ENSO. Their study only made a simple correlation but did not explain how ENSO influences Antarctic extreme precipitation. In this study, we utilize six decades (1963–2023) of daily in situ observations of precipitation from Russia's Novolazarevskaya Station, located in the Schirmacher Oasis of DLM, to investigate the characteristics of extreme precipitation, focusing on interannual variability and trends in extreme precipitation days. Additionally, we evaluate the interdecadal variability in the relationship between ENSO and the interannual variability of extreme precipitation days.

2. Study Region, Data, and Methods

Russian Novolazarevskaya Station (70°46′S, 11°50′E, elevation 119 m above mean sea level) (Figure 1) is located at the southeastern tip of the Schirmacher oasis and on the shores of Lake Stantsionnoye in DML, approximately 80 km from the Lazarev Sea. Positioned near the edge of the ice shelf, the station is surrounded by relatively ice-free terrain, making it one of the few areas of exposed rock in this otherwise ice-covered region.

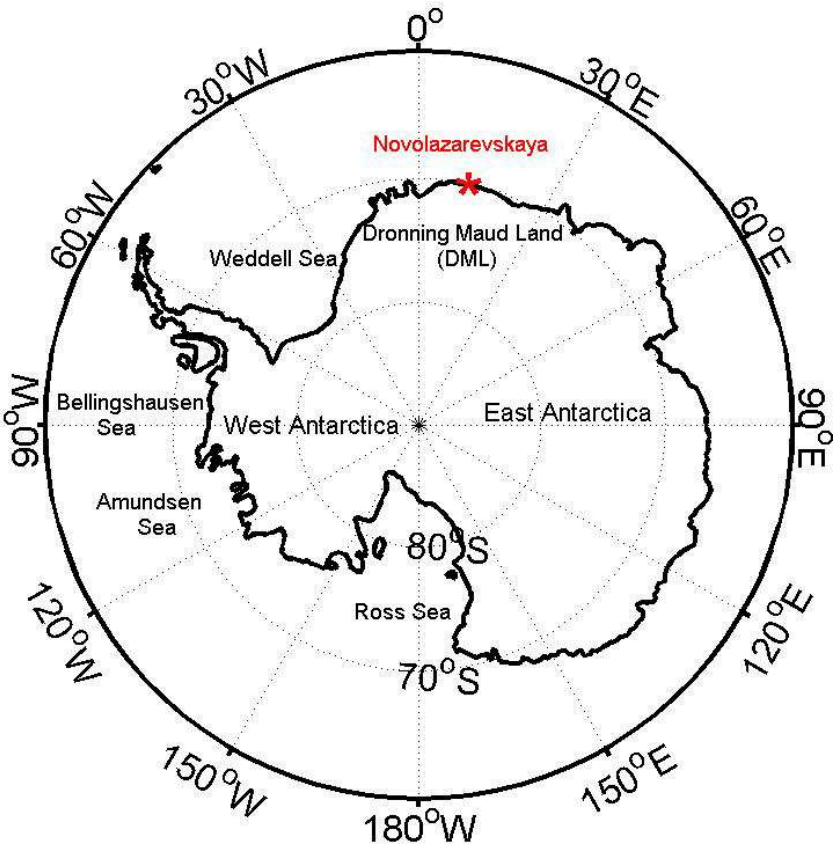

Figure 1. The map of the study region. The asterisk indicates the location of Russia's Novolazarevskaya Station in East Antarctica.

Precipitation has been measured twice a day (at 06 and 18 GMT) at the station using the Tretyakov precipitation gauge [36], which ensures the homogeneity of the time series of daily precipitation. The sum of observations per day is used as daily precipitation. Our analysis utilized daily data from January 1963 to December 2023. An extreme precipitation day was defined as a day when the daily precipitation amount exceeded the 90th percentile of the entire period [6], corresponding to a threshold of 13 mm day-1. During the 1963–2023 period, 325 extreme precipitation days were recorded.

To analyze the synoptic conditions related to extreme precipitation days, we utilized the latest version (version 5) of the European Centre for Medium-Range Weather Forecasts (ECMWF) ReAnalysis (ERA5) [37]. ERA5 data provide higher horizontal resolution (0.25° latitude × 0.25° longitude), more vertical levels (137), and a longer time span (from 1950 to the present) compared to its predecessors, such as ERA-Interim. ERA5 surpasses other reanalysis datasets in accurately representing Antarctic atmospheric variables [38–41], a feature that is particularly important for our analyses. The atmospheric variables obtained from the ERA5 reanalysis and utilized in the study include 500 hPa geopotential height, 500 hPa vertical velocity, mean sea level pressure, total column water vapor, and vertically integrated water vapor flux. Another key variable for our analyses, sea surface temperature (SST) anomalies, was obtained from the U.S. National Oceanic and Atmospheric Administration (NOAA) Extended Reconstructed SST V5 dataset [42]. The austral winter semester refers to May–October.

The statistical methods employed in this study include Pearson correlation, composite, and regression analyses, with statistical significance assessed using a two-tailed Student's *t*-test. The Niño 3.4 index was obtained from the website (https://psl.noaa.gov/data/climateindices/list/#TSA, accessed on 12 July 2024), and the SAM index was obtained from (http://lijianping.cn/dct/page/65609, accessed on 12 July 2024) [43].

The Pearson correlation of two variables $x(x_1, x_2, \cdots, x_n), y(y_1, y_2, \cdots, y_n)$ is calculated according to Equation (1),

$$r = \frac{\sum_{i=1}^{n} (x_i - \overline{x})(y_i - \overline{y})}{\sqrt{\sum_{i=1}^{n} (x_i - \overline{x})} \sqrt{\sum_{i=1}^{n} (y_i - \overline{y})}}, \quad (1)$$

where r is the Pearson correlation coefficient, and the bar indicates the average value of two variables.

A linear regression between $x(x_1, x_2, \cdots, x_n), y(y_1, y_2, \cdots, y_n)$ is conducted according to Equation (2),

$$y_i = \alpha + \beta x_i + \varepsilon_i, \quad (2)$$

where α is the intercept, β is the slope, and ε_i is a residual term. A least square is employed to minimize the sum of squared residuals. The residuals are tested for temporal independence using the autocorrelation function. In this study, y variables are oceanic and atmospheric variables such as SST and 200 hPa geopotential height; x variables refer to the normalized Niño 3.4 index and the normalized number of days with extreme precipitation. In the Section 3, the regression maps show the spatial pattern of the β value at each grid point for a given oceanic or atmospheric variable, suggesting the changes in the y variables related to the changes in the x variables.

The Theil–Sen Median method is utilized to estimate the trend in a time series $x(x_1, x_2, \cdots, x_n)$ according to the following Equation (3):

$$\rho = median(\frac{x_j - x_i}{j - i}) 1 < i < j < n, \quad (3)$$

where n is the length of the time series, in this study, n = 61; ρ is the trend of the time series $x(x_1, x_2, \cdots, x_n)$; and $\rho > 0$ and $\rho < 0$ indicate the increased and decreased trend, respectively. The statistical significance of the Theil–Sen Median trend is assessed by the Mann–Kendall test.

3. Results

3.1. Precipitation Characteristics

Over the past six decades (1963–2023), the average annual precipitation at Novolazarevskaya Station was 237.9 mm water equivalent. The annual precipitation exhibits substantial interannual variability, with the highest value recorded in 1974 at 579.8 mm and the lowest in 1968 at 26.8 mm (Figure 2a). There is a decreasing trend in annual precipitation, although it is not statistically significant. The average annual number of days with precipitation is 52.8, also showing considerable interannual variability. The highest number of precipitation days occurred in 1963 (89 days), while the fewest occurred in 1978 (17 days) (Figure 2b). Similarly, the decreasing trend in the number of precipitation days is not statistically significant. The SAM is the dominant mode of atmospheric circulation variability in the southern mid-to-high latitudes [44]. The time series of both the annual precipitation amount and the number of precipitation days show no significant correlation with the annual SAM index over the study period.

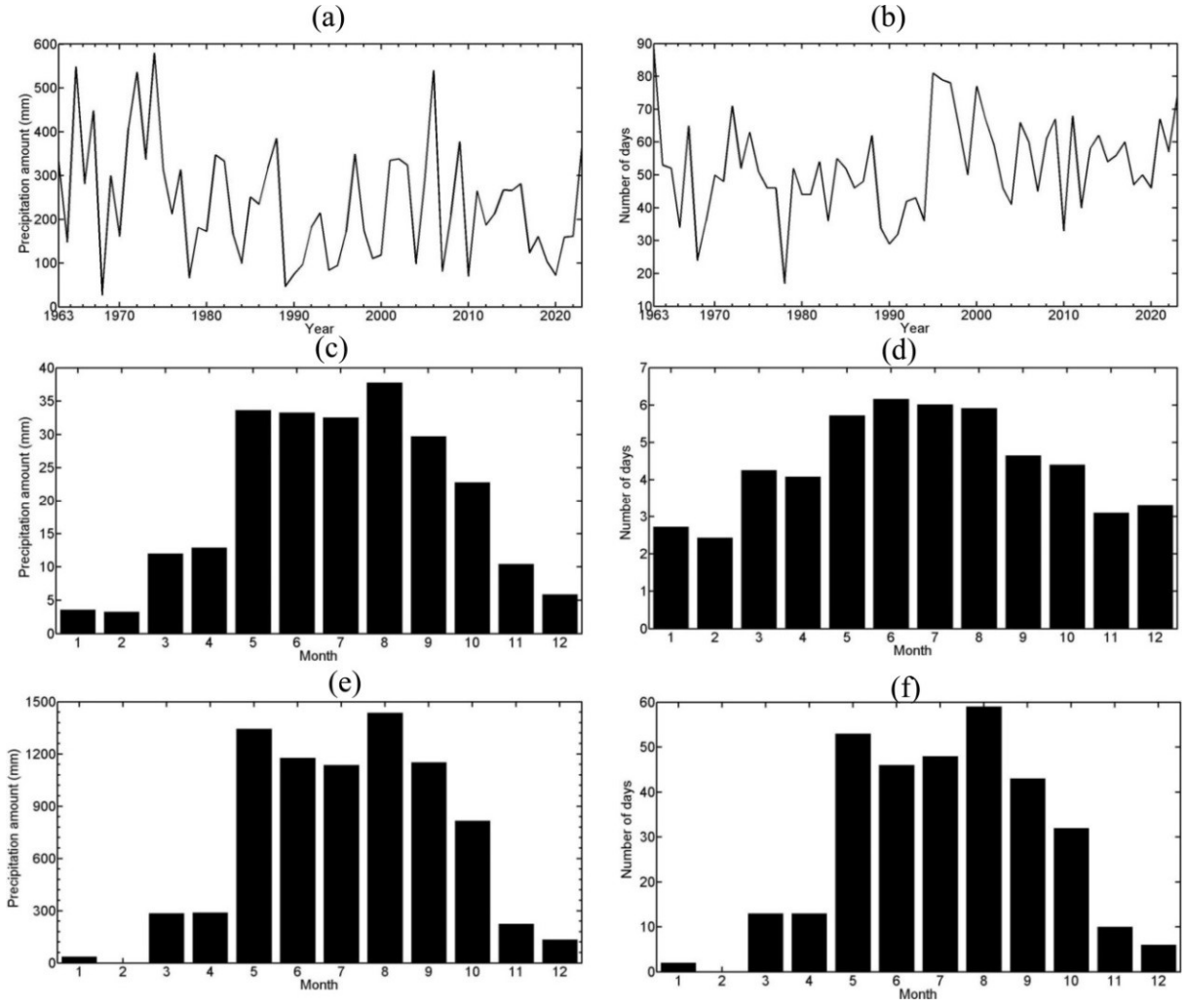

Figure 2. Time series of (**a**) annual precipitation amount (mm) and (**b**) annual number of days with precipitation (day) for the 1963–2023 period; the 63-yr averaged (**c**) amount (mm) and (**d**) number of days (day) of monthly precipitation for the 1963–2023 period; the 63-yr total (**e**) amount (mm) and (**f**) number of days (day) of monthly extreme precipitation for the 1963–2023 period.

In addition to interannual variability, precipitation at Novolazarevskaya Station exhibits seasonal variation (Figure 2c). August typically receives the most precipitation, while February receives the least. The austral winter semester (May–October) accounts

for 79.8% of the annual precipitation total. The number of precipitation days displays less seasonal variation compared to the precipitation amount (Figure 2d). The highest number of precipitation days occurs in June, while February experiences the fewest. A total of 62.3% of precipitation days occur during the austral winter semester.

From 1963 to 2023, the climatological average number of days with extreme precipitation at Novolazarevskaya Station was 5.3 days per year, accounting for 10% of all precipitation days. The average extreme precipitation amount was 131.7 mm per year, representing 55.4% of the total annual precipitation. This is broadly consistent with the findings of Turner et al. [6], who suggested that 40% of annual precipitation arises from just 10% of the largest daily precipitation events. Annual extreme precipitation amounts are closely linked to the number of extreme precipitation days, with a high correlation coefficient (r = 0.96). The annual number of days with extreme precipitation shows a significant decreasing trend of −0.07 days per year ($p < 0.05$), while the annual extreme precipitation amount exhibits a significant declining trend of −1.6 mm per year ($p < 0.05$) (Figure 3a,b). Unlike the annual precipitation amount and the number of precipitation days, which show no significant correlation with the annual SAM index, both the number of extreme precipitation days and the extreme precipitation amount are significantly correlated with the annual SAM index (Figure 3c), with correlation coefficients of −0.39 ($p < 0.02$) and −0.38 ($p < 0.02$), respectively. The annual SAM index has a significantly positive trend of 0.04 ($p < 0.05$) over the past 60 years. However, when trends are removed, these correlations become non-significant (r = −0.16, $p > 0.05$ and r = −0.19, $p > 0.05$). The ratio of extreme precipitation to total annual precipitation has decreased over the past six decades with a trend of −0.6% ($p < 0.05$) (Figure 3d). The interannual variance in extreme precipitation amounts explains 74.5% of the variance in total annual precipitation, further supporting the findings of Turner et al. [6]. Both the amount of extreme precipitation and the number of extreme precipitation days exhibit strong seasonal variability (Figure 2e,f). Notably, 86.5% of extreme precipitation days and 87.9% of extreme precipitation amounts occur during the austral winter semester, with the highest number of extreme precipitation days occurring in August.

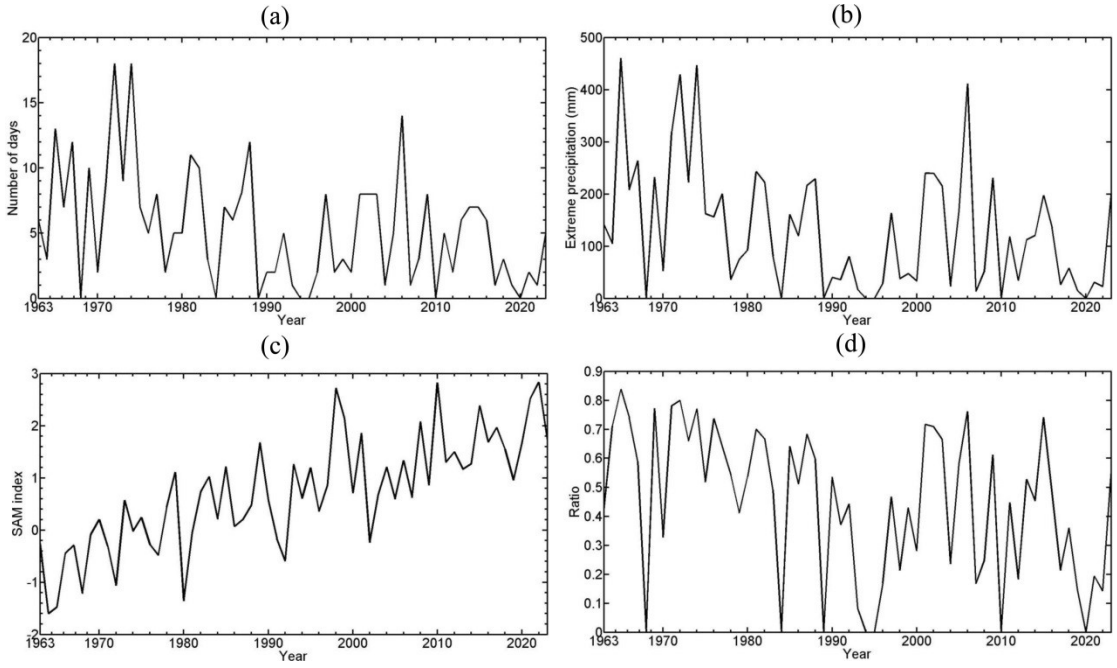

Figure 3. Time series of annual (**a**) number of days and (**b**) amount of extreme precipitation, SAM index (**c**), and the ratio of extreme precipitation to the total precipitation (**d**).

3.2. Synoptic Patterns Associated with Extreme Precipitation

To explain the extreme precipitation characteristics observed at Novolazarevskaya Station, we performed a composite analysis of atmospheric variables during the 325 extreme precipitation days (Figure 4). Both the anomalous 500 hPa geopotential heights and mean sea level pressures display a dipole structure over the region, with positive anomalies to the west and negative anomalies to the east of the station location (Figure 4a,b). This pattern was also observed in the composite analysis of extreme precipitation at the Progress and Casey stations [24,25]. The dipole structure of anomalous heights supports the formation of a southward water vapor flux over the area of the station, flanked by a northward flux to the west of the negative height center and to the east of the positive height center (Figure 4c). Negative vertical velocity (ω, the rate of pressure change with time in isobaric coordinates) anomalies, indicating upward motion, are consistent with the southward water vapor flux, while positive vertical velocity anomalies, associated with downward motion, indicate the opposite (Figure 4d). The strong upward motion over the station condenses the water vapor, leading to extreme precipitation events. The small wave pattern in the vertical velocity field may be linked to gravity waves triggered by the topography of the coastal continent [16,17].

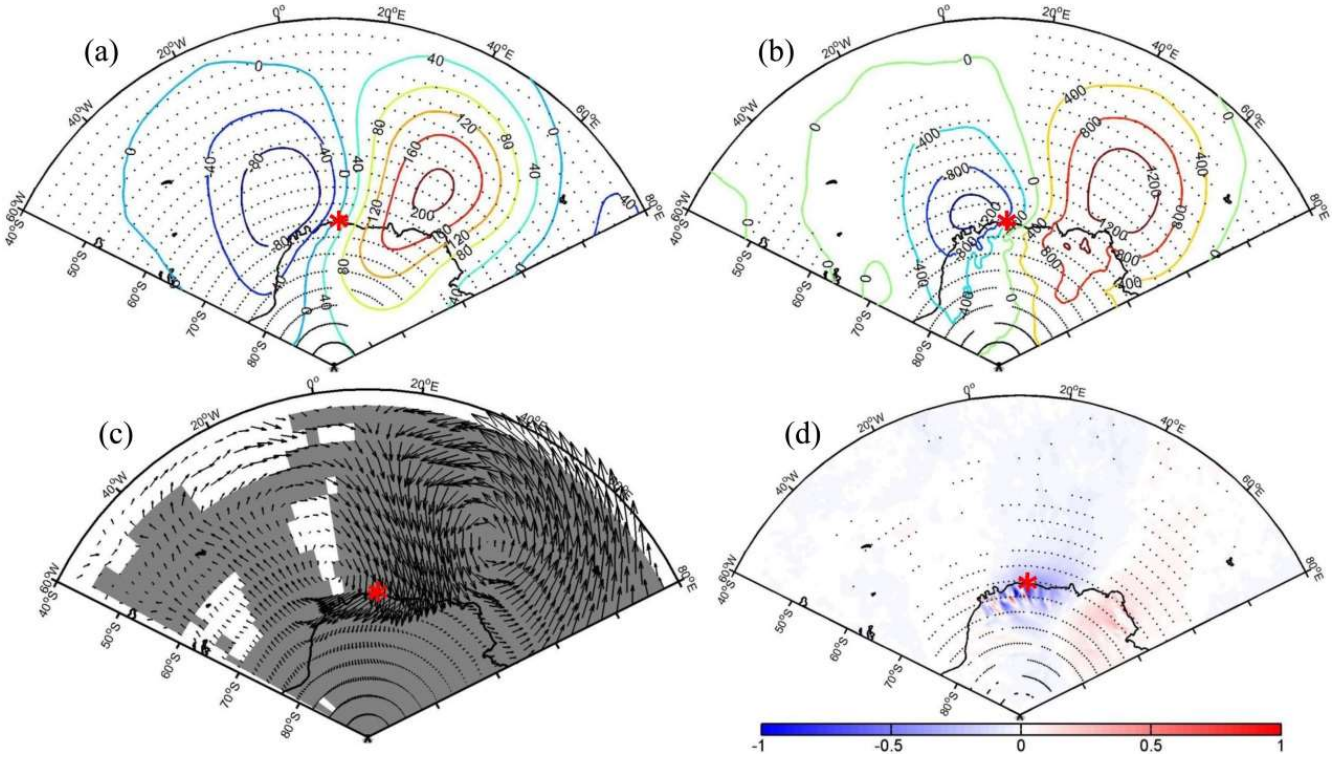

Figure 4. Composite maps of anomalous 500 hPa geopotential heights (gmp) (**a**), mean sea level pressure (MSLP) (Pascal) (**b**), vertically integrated water vapor flux (kg m^{-1} s^{-1}) (**c**), and 500 hPa vertical velocity (Pa s^{-1}) (**d**) for extreme precipitation occurrences. Dotted (shaded) regions indicate above 95% confidence level. Red asterisks indicate the location of Russian stations.

3.3. Interannual and Decadal Variability in Extreme Precipitation Occurrences

Extreme precipitation primarily occurs during the austral winter semester (May–October), with the number of extreme precipitation days in this period highly correlated with the total number of extreme precipitation days in a given year ($r = 0.97$, $p < 0.01$). The detrended number of extreme precipitation days from May to October also shows a significant correlation with the detrended Niño 3.4 index for the same period ($r = 0.29$, $p < 0.05$) (Figure 5a). To further explore the relationship between ENSO and the extreme

precipitation occurrences observed at Novolazarevskaya Station, we conducted a regression analysis of atmospheric and SST anomalies onto the normalized and detrended time series of extreme precipitation days over the past six decades.

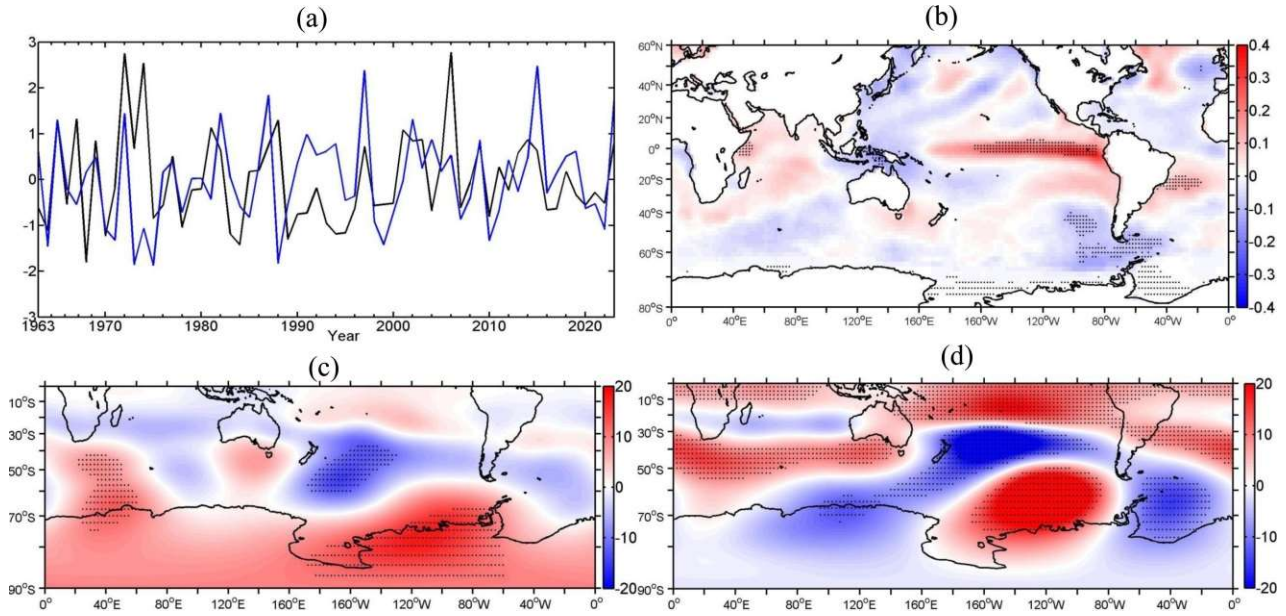

Figure 5. Time series of normalized number of days with extreme precipitation in May-October (black line) and Niño 3.4 index (blue line) (**a**), the regression map of SST anomalies (°C) (**b**) and 200 hPa geopotential height anomalies (gmp) (**c**) onto the normalized number of days with extreme precipitation, the regression map of 200 hPa geopotential height anomalies (gmp) (**d**) onto the normalized Niño 3.4 index.

The SST anomalies associated with extreme precipitation occurrences indicate an El Niño state in the tropical Pacific Ocean (Figure 5b). Additionally, significantly negative SST anomalies are present over the southeastern Pacific Ocean and southern high-latitude seas. El Niño is known to trigger a wavetrain referred to as the PSA mode [45], which affects atmospheric conditions in the Southern Ocean and Antarctic continent [46–49]. Similarly, the El Niño state excites a wavetrain that propagates southeastward into the Amundsen and Bellingshausen Seas and then eastward into the Southern Atlantic and Indian sectors of the Southern Ocean (Figure 5c). This wavetrain generates a dipole pattern of negative (positive) anomalies northwest (southeast) of Novolazarevskaya Station at the 500 hPa level (Figure 6a). The mean sea level pressure anomalies display a similar structure to the 500 hPa geopotential height anomalies (Figure 6b). These height anomalies drive southward, vertically integrated water vapor transport over Novolazarevskaya Station (Figure 6c), promoting extreme precipitation. Concurrent upward motion anomalies further support the condensation of water vapor (Figure 6d), facilitating the formation of extreme precipitation. While these regression results align with the composite analysis, there are differences in the locations of the 500 hPa height and mean sea level pressure anomaly centers.

To further investigate the connection to ENSO, we regressed SST and atmospheric anomalies directly onto the normalized and detrended Niño 3.4 index over the past six decades. A similar wavetrain is triggered by positive SST anomalies in the central and eastern Pacific Ocean; however, the location and extent of the height anomalies differ from the previously discussed wavetrain (Figure 5d). A dipole structure of 500 hPa geopotential heights and mean sea level pressure also emerges (Figure 7a,b), but the height anomalies are stronger than those found in the regression map of normalized extreme precipita-

tion days (Figure 6a). The northeastward shift in the positive height anomalies results in weaker southward vertically integrated water vapor transport over Novolazarevskaya Station (Figure 7c). The vertical motion anomalies also contribute to extreme precipitation formation (Figure 7d). Together, these regression results (Figures 7–9) establish a teleconnection between ENSO and the frequency of extreme precipitation occurrences at Novolazarevskaya Station, driven by the atmospheric circulation anomalies associated with the wavetrain.

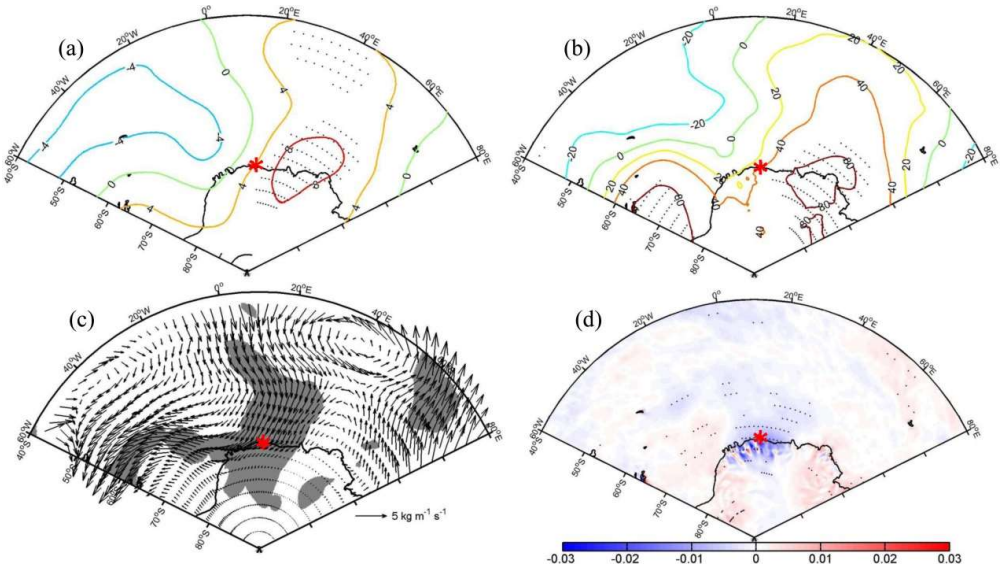

Figure 6. Regression map of anomalous 500 hPa geopotential heights (gmp) (**a**), mean sea level pressure (Pascal) (**b**), vertically integrated water vapor flux (kg m^{-1} s^{-1}) (**c**), and 500 hPa vertical velocity (Pa s^{-1}) (**d**) onto the normalized number of days with extreme precipitation over the past six decades. Dotted (shaded) regions indicate above 95% confidence level. Red asterisks indicate the location of Russian stations.

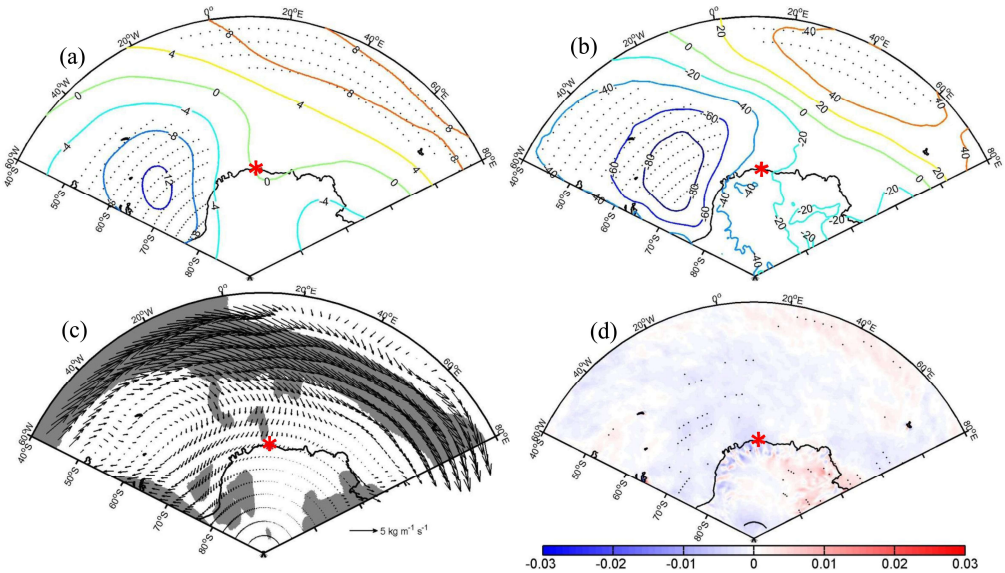

Figure 7. Regression map of anomalous 500 hPa geopotential heights (gmp) (**a**), mean sea level pressure (Pascal) (**b**), vertically integrated water vapor flux (kg m^{-1} s^{-1}) (**c**), and 500 hPa vertical velocity (Pa s^{-1}) (**d**) onto the normalized Niño 3.4 index over the past six decades. Dotted (shaded) regions indicate above 95% confidence level. Red asterisks indicate the location of Russian stations.

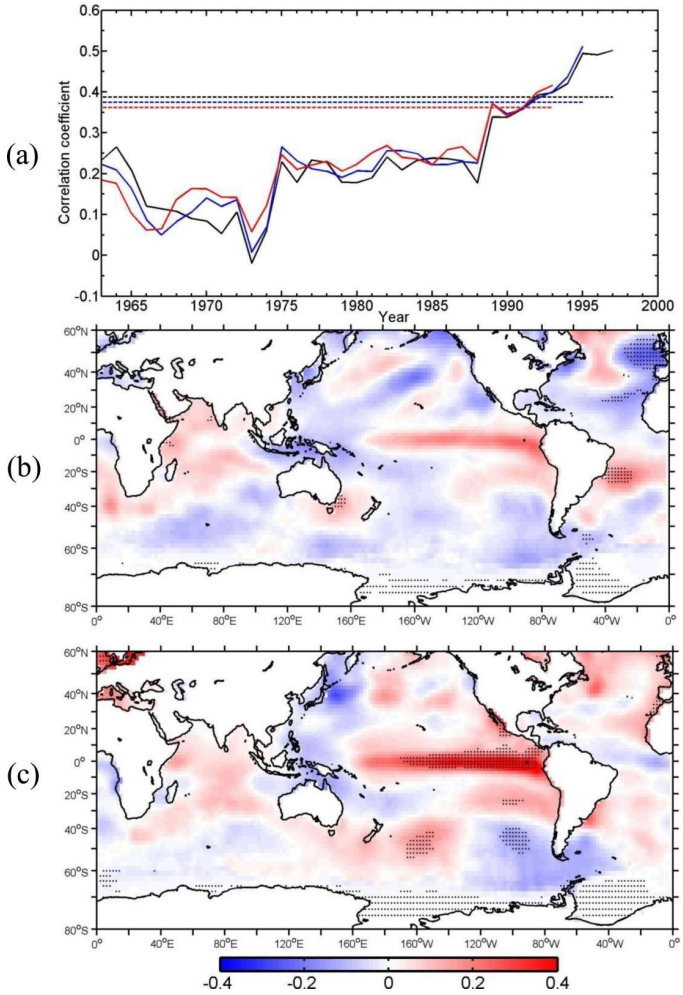

Figure 8. The moving correlation of the Nino 3.4 index and the number of days with extreme precipitation with the moving windows of 26 (red), 28 (blue), and 30 (black) years (**a**). The dashed lines indicate $p = 0.05$ lines. The regression maps of SST anomalies (°C) onto the normalized number of days with extreme precipitation for the 1963–1992 (**b**) and 1993–2023 (**c**) periods.

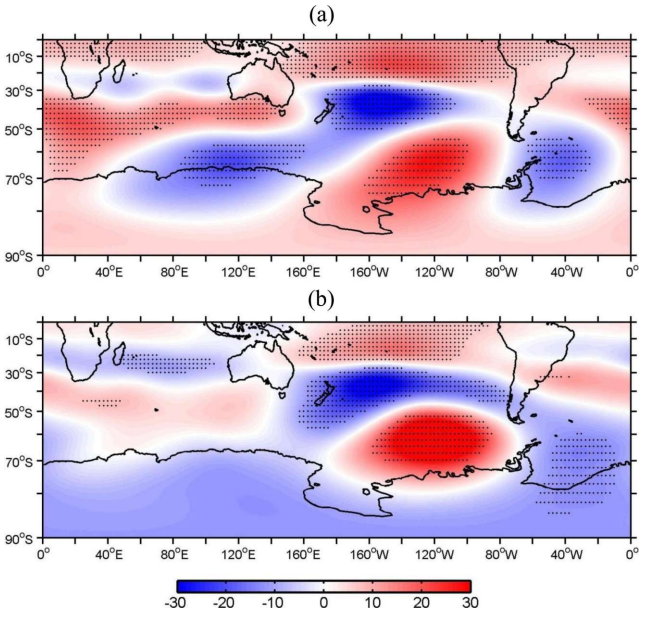

Figure 9. The regression maps of 200 hPa geopotential height (gmp) anomalies onto the normalized Niño 3.4 index for the 1963–1992 (**a**) and 1993–2023 (**b**) periods.

The teleconnection, however, has been inconsistent over the past six decades. We calculated the moving correlation between the detrended Niño 3.4 index and the detrended number of extreme precipitation days in the winter semester using 26-, 28-, and 30-year windows (Figure 8a). Across all three windows, the correlation coefficients increase from near zero to 0.41, 0.51, and 0.50, respectively. The point where the correlation reaches significance ($p = 0.05$) occurs around 1992/1993. From 1963 to 1992, the correlation was weak ($r = 0.18$, $p > 0.05$), whereas from 1993 to 2023, it strengthened significantly ($r = 0.44$, $p < 0.02$). To explore this shift, we regressed winter semester SST anomalies onto the time series of extreme precipitation days for both periods (Figure 8b,c). During the latter period, significant SST anomalies in the mid-to-low latitudes associated with extreme precipitation are primarily located in the tropical and southern Pacific Oceans. In contrast, during the earlier period, significant SST anomalies are found in the Atlantic Ocean. This difference explains why a pronounced eastern Pacific El Niño signal is evident in the latter period but absent in the former.

We also conducted separate regressions of atmospheric variables onto the Niño 3.4 index for the two periods (Figures 9–11). While the 200 hPa geopotential height anomalies are similar across both periods and resemble those for the entire 60-year dataset, notable differences emerge over the southern Atlantic, Indian Oceans, and Antarctic continent. In the latter period, the negative height anomalies over the Weddell Sea shift eastward, while the positive anomalies over the Indian sector of the Southern Ocean weaken. Although the anomalous 500 hPa geopotential heights and sea level pressure are stronger during the earlier period, the positive anomaly centers in both height and pressure divert water vapor transport eastward, reducing the moisture flux through Novolazarevskaya Station. In contrast, in the latter period, negative 500 hPa height and sea level pressure anomalies channel water vapor toward the station from the northeast. Upward motion during the latter period (-0.0029 Pa s^{-1}) is also stronger than in the earlier period (-0.0015 Pa s^{-1}). These variations in the location and strength of height anomalies related to the wavetrain help explain the differing correlations between ENSO and extreme precipitation occurrences at Novolazarevskaya Station.

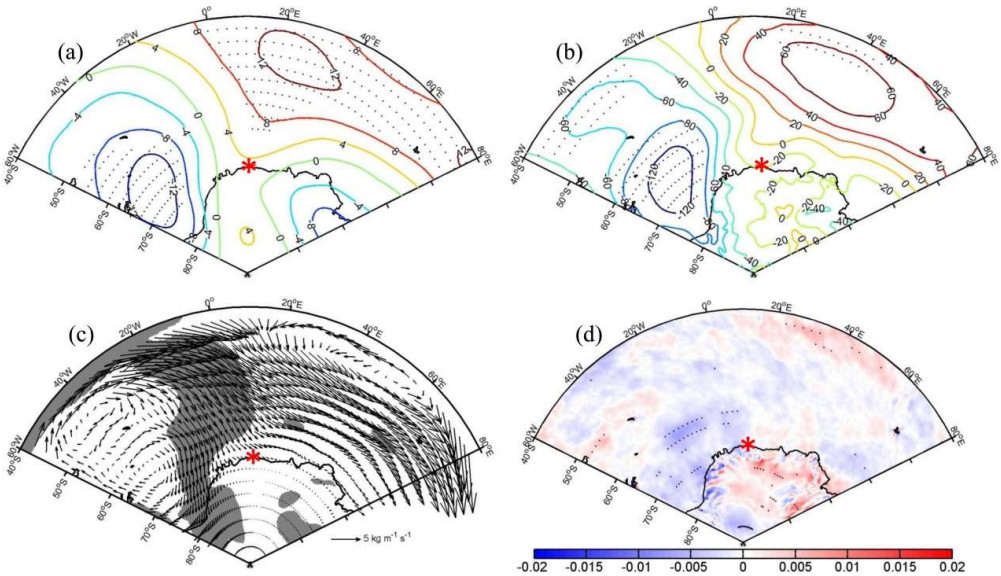

Figure 10. Regression maps of anomalous 500 hPa geopotential heights (gmp) (**a**), mean sea level pressure (Pascal) (**b**), vertically integrated water vapor flux (kg m^{-1} s^{-1}) (**c**), and 500 hPa vertical velocity (Pa s^{-1}) (**d**) onto the normalized Niño 3.4 index in May-October for the 1963–1992 period. Dotted (shaded) regions indicate above 95% confidence level. Red asterisks indicate the location of Russian stations.

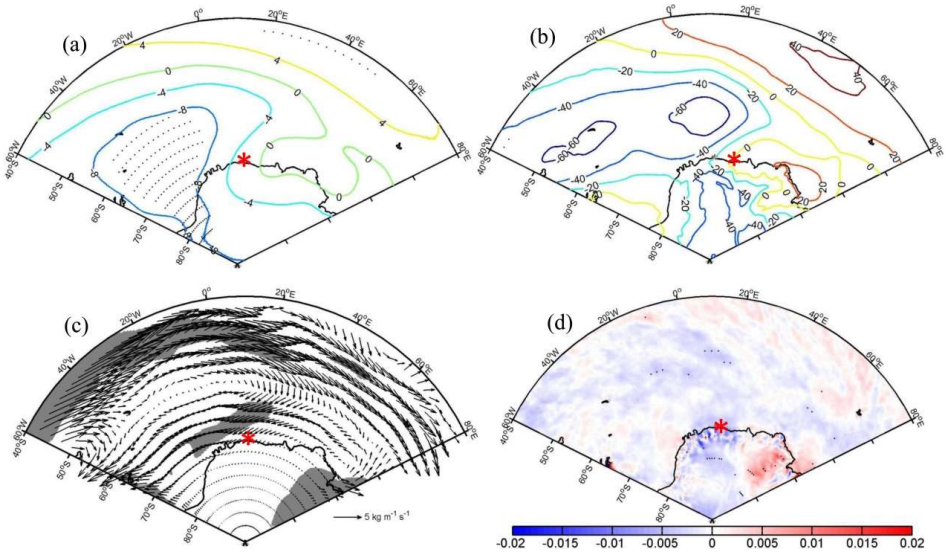

Figure 11. Regression maps of anomalous 500 hPa geopotential heights (gmp) (**a**), mean sea level pressure (Pascal) (**b**), vertically integrated water vapor flux (kg m^{-1} s^{-1}) (**c**), and 500 hPa vertical velocity (Pa s^{-1}) (**d**) onto the normalized Niño 3.4 index in May-October for the 1993–2022 period. Dotted (shaded) regions indicate above 95% confidence level. Red asterisks indicate the location of Russian stations.

3.4. Drivers of the Decreasing Trend in Extreme Precipitation

We observe a decreasing trend in both the annual number of days and the total amount of extreme precipitation. This decline can be explained by changes in atmospheric circulation patterns during the austral winter (Figure 12). Anomalous high pressure to the west and low pressure to the east of the station (Figure 12a), combined with negative sea level pressure anomalies to the north, drive northward water vapor transport over the station. This pattern is unfavorable for increasing the occurrence of extreme precipitation. Additionally, the observed trend in downward motion over the station further reduces the likelihood of extreme precipitation events. The trends in 500 hPa geopotential height and mean sea level pressure may be connected to the shift toward the positive phase of the SAM (Figure 3c).

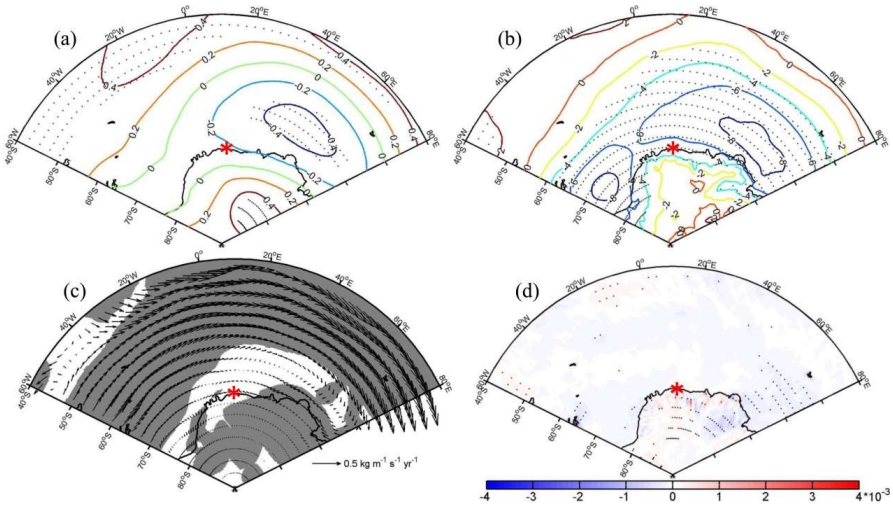

Figure 12. Trends in anomalous 500 hPa geopotential heights (gmp yr^{-1}) (**a**), mean sea level pressure (Pascal yr^{-1}) (**b**), vertically integrated water vapor flux (kg m^{-1} $s^{-1}yr^{-1}$) (**c**), and 500 hPa vertical velocity (Pa s^{-1} yr^{-1}) (**d**). Dotted (shaded) regions indicate above 95% confidence level. Red asterisks indicate the location of Russian stations.

4. Conclusions and Discussion

Using daily precipitation data from 1963 to 2023 from Russia's Novolazarevskaya Station, we analyzed the characteristics of extreme precipitation in the Dronning Maud Land region (20°W to 45°E) in East Antarctica. Additionally, we examined the synoptic conditions associated with extreme precipitation in this region, as well as the interannual variability, trends in occurrence frequency, and their teleconnection to ENSO.

Annual and extreme precipitations at Novolazarevskaya Station primarily occur during the austral winter semester (May–October) (>80%). Extreme precipitation accounts for 10% of all precipitation days and 55% of the total annual precipitation amount. The synoptic pattern associated with extreme precipitation is characterized by a dipole structure, with negative height anomalies to the west and positive anomalies to the east of the station, facilitating the transport of water vapor toward the region. Over the past six decades, both the amount and frequency of extreme precipitation, along with its ratio to total annual precipitation, have exhibited a decreasing trend. This decline may be linked to reduced upward atmospheric motion and a shift in northward water vapor flux, both of which are influenced by changes in atmospheric height patterns. On an interannual timescale, the frequency of extreme precipitation days is positively correlated with the Niño 3.4 index during the austral winter semester. However, this relationship fluctuates on a decadal scale, with a weaker correlation observed from 1963 to 1992 and a stronger one from 1993 to 2023. These shifts in correlation are tied to variations in the wavetrain patterns associated with ENSO during these two periods.

The synoptic dipole structure associated with extreme precipitation events is consistent with similar findings at Progress station in the Prydz Bay region, Casey Station in Wilkes Land [24,25] and in Dronning Maud Land [18,21,23,35]. This dipole structure frequently forms over the Southern Ocean and is influenced by low-frequency oscillations such as the PSA mode [23], as observed in Figure 6. Our findings contrast with the increasing trend in extreme precipitation reported by Turner et al. [6] and Simon et al. [35]. This discrepancy may be likely due to differences in the data and study periods. While our analysis spans the 1963–2023 period using observational data, Turner et al. [6] and Simon et al. [35] relied on regional model data (RACMO2) and reanalysis data (ERA5) over the past 40 years. The trend in annual extreme precipitation amounts at the station for 1979 to 2016 is 0.58 mm year^{-1} ($p > 0.05$), which agrees with the results of Turner et al. [6] and Simon et al. [35]. There is a significant increasing trend in annual surface air temperature at the station (0.01 °C year^{-1}, $p < 0.05$). But there is no significant correlation between annual mean air temperature and annual number of extreme precipitation days and the total amount of extreme precipitation. Wille et al. [12] and Turner et al. [6] noted that ARs are responsible for 40–60% of their total annual precipitation from daily extreme precipitation events. According to a 90th percentile threshold of integrated water vapor transport [50], ARs are associated with 57.4% of the extreme precipitation days. ARs using a 98th percentile threshold are responsible for 10.5% of the extreme precipitation days.

The positive correlation between extreme precipitation and the Niño 3.4 index during austral winter in Dronning Maud Land is consistent with findings by Turner et al. [6] for austral spring. To our knowledge, we are the first to identify the interdecadal variability in this relationship, which results from different wavetrains excited by positive tropical Pacific SST anomalies. Recent studies suggest that this variability may be linked to the interdecadal shifts in the Atlantic Multidecadal Oscillation (AMO) [51] and the increasing frequency of central Pacific El Niño events [52]. However, the specific causes of the interdecadal variability in the ENSO-Antarctic extreme precipitation relationship require further investigation.

Measuring Antarctic precipitation is challenging due to strong winds, low temperatures, and the influence of blowing snow. Previous studies have confirmed that blowing snow has minimal impact on the interannual variability and trends of extreme precipitation days [24]. Increasing the threshold for extreme precipitation from the 90th to the 95th percentile of the entire period yields similar conclusions. However, the limited number of extreme precipitation days (162) restricts our ability to thoroughly analyze its interannual variability.

Despite potential biases in precipitation measurements that may affect the magnitude of extreme precipitation amounts, our findings provide a valuable reference for interpreting ice core data and estimating surface mass balance in Dronning Maud Land, East Antarctica. Furthermore, our conclusions offer insights into the future of extreme precipitation in this region, particularly in relation to atmospheric circulation changes driven by a strengthening SAM index due to increasing greenhouse gas emissions. The interdecadal variability of the relationship between extreme precipitation and ENSO can advance the understanding of the impact of tropical SST anomalies on the Antarctic climate and lay a statistical foundation for the prediction of Antarctic precipitation.

Author Contributions: Conceptualization, L.Y.; Formal analysis, C.S.; Data curation, S.J.; Writing—review & editing, S.Z.; Supervision, B.S. All authors have read and agreed to the published version of the manuscript.

Funding: This study is financially supported by the National Key R&D Program of China (2024YFF0506601).

Data Availability Statement: The monthly SST data from the U.S. NOAA Extended Reconstructed Sea Surface Temperature (ERSST) version 5 (ERSST v5) are available online (https://www1.ncdc.noaa.gov/pub/data/cmb/ersst/v5/netcdf/). The ERA5 reanalysis data are available from the website (https://doi.org/10.24381/cds.6860a573). Daily precipitation data at Novolazarevskaya Station is available upon request to the corresponding author.

Acknowledgments: We thank the European Centre for Medium-Range Weather Forecasts (ECMWF) for making the ERA5 data available to the public and the Russian station for providing precipitation data.

Conflicts of Interest: The authors declare no conflict of interest.

References

1. Bromwich, D.H. Snowfall in high southern latitudes. *Rev. Geophys.* **1988**, *26*, 149–168. [CrossRef]
2. Shepherd, A.; Wingham, D. Recent sea-level contributions of the Antarctic and Greenland ice sheets. *Science* **2007**, *315*, 1529–1532. [CrossRef] [PubMed]
3. Davison, B.J.; Hogg, A.E.; Rigby, R.; Veldhuijsen, S.; van Wessem, J.M.; van den Broeke, M.R.; Holland, P.R.; Selley, H.L.; Dutrieux, P. Sea level rise from West Antarctic mass loss significantly modified by large snowfall anomalies. *Nat. Commun.* **2023**, *14*, 1479. [CrossRef]
4. Thomas, E.R.; Van Wessem, J.M.; Roberts, J.; Isaksson, E.; Schlosser, E.; Fudge, T.J.; Vallelonga, P.; Medley, B.; Lenaerts, J.; Bertler, N.; et al. Review of regional Antarctic snow accumulation over the past 1000 years. *Clim. Past* **2017**, *113*, 1491–1513. [CrossRef]
5. Jackson, S.L.; Vance, T.R.; Crockart, C.; Moy, A.; Plummer, C.; Abram, N.J. Climatology of the Mount Brown South ice core site in East Antarctica: Implications for the interpretation of a water isotope record. *Clim. Past* **2023**, *19*, 1653–1675. [CrossRef]
6. Turner, J.; Phillips, T.; Thamban, M.; Rahaman, W.; Marshall, G.J.; Wille, J.D.; Favier, V.; Winton, V.H.L.; Thomas, E.; Wang, Z.; et al. The dominant role of extreme precipitation events in Antarctic snowfall Variability. *Geophys. Res. Lett.* **2019**, *46*, 3502–3511. [CrossRef]
7. Casado, M.; Münch, T.; Laepple, T. Climatic information archived in ice cores: Impact of intermittency and diffusion on the recorded isotopic signal in Antarctica. *Clim. Past* **2020**, *16*, 1581–1598. [CrossRef]
8. Servettaz, A.P.M.; Orsi, A.J.; Curran, M.A.; Moy, A.D.; Landais, A.; Agosta, C.; Winton, V.H.L.; Touzeau, A.; McConnell, J.R.; Werner, M.; et al. Snowfall and water stable isotope variability in East Antarctica controlled by warm synoptic events. *J. Geophys. Res.* **2020**, *125*, e2020JD032863. [CrossRef]

9. Gorodetskaya, I.V.; Tsukernik, M.; Claes, K.; Ralph, M.F.; Neff, W.D.; van Lipzig, N.P.M. The role of atmospheric rivers in anomalous snow accumulation in East Antarctica. *Geophys. Res. Lett.* **2014**, *41*, 6199–6206. [CrossRef]
10. Terpstra, A.; Gorodetskaya, I.V.; Sodemann, H. Linking sub-tropical evaporation and extreme precipitation over East Antarctica: An atmospheric river case study. *J. Geophys. Res.* **2021**, *126*, e2020JD033617. [CrossRef]
11. Adusumilli, S.; Fish, M.A.; Fricker, H.A.; Medley, B. Atmospheric river precipitation contributed to rapid increases in surface height of the West Antarctic Ice Sheet in 2019. *Geophys. Res. Lett.* **2021**, *48*, e2020GL091076. [CrossRef]
12. Wille, J.D.; Favier, V.; Gorodetskaya, I.V.; Agosta, C.; Kittel, C.; Beeman, J.C.; Jourdain, N.C.; Lenaerts, J.T.; Codron, F. Antarctic atmospheric river climatology and precipitation impacts. *J. Geophys. Res.* **2021**, *126*, e2020JD033788. [CrossRef]
13. Gao, Q.; . Sime, L.C.; McLaren, A.; Bracegirdle, T.J.; Capron, E.; Rhodes, R.H.; Steen-Larsen, H.C.; Shi, X.; Werner, M. Evaporative Controls of precipitation evaporation in Antarctica: An model study of ECHAM6 using innovative diagnostics of water indicators. *Cyosphere* **2024**, *18*, 683–703. [CrossRef]
14. Jullien, N.; Vignon, É.; Sprenger, M.; Aemisegger, F.; Berne, A. Synoptic conditions and atmospheric moisture pathways associated with virga and precipitation over coastal Adélie Land in Antarctica. *Cryosphere* **2020**, *14*, 1685–1902. [CrossRef]
15. Messmer, M.; Simmonds, I. Global analysis of cyclone-induced compound precipitation and wind extreme events. *Weather Clim. Extrem.* **2021**, *32*, 100324. [CrossRef]
16. Fujita, S.; Holmlund, P.; Andersson, I.; Brown, I.; Enomoto, H.; Fujii, Y.; Fujita, K.; Fukui, K.; Furukawa, T.; Hansson, M.; et al. Spatial and temporal variability of snow accumu-lation rate on the East Antarctic ice divide between Dome Fuji and EPICA DML. *Cryosphere* **2011**, *5*, 1057–1081. [CrossRef]
17. Gehring, J.; Vignon, É.; Billault-Roux, A.-C.; Ferrone, A.; Protat, A.; Alexander, S.; Alexis, B. Orographic flow influence on precipitation during an atmospheric river event at Davis, Antarctica. *J. Geophys. Res.* **2022**, *127*, e2021JD035210. [CrossRef]
18. Welker, C.; Martius, O.; Froidevaux, P.; Reijmer, C.H.; Fischer, H. A climatological analysis of high-precipitation events in Dronning Maud Land, Antarctica, and associated large-scale atmospheric conditions. *J. Geophys. Res. Atmos.* **2014**, *119*, 11932–11954. [CrossRef]
19. Wang, S.; Ding, M.; Liu, G.; Chen, W. Progress and mechanisms of persistent extreme rainfall events in the Antarctic Peninsula during austral summer. *J. Clim.* **2022**, *35*, 3642–3657. [CrossRef]
20. Wang, S.; Ding, M.; Liu, G.; Li, G.; Chen, W. Blocking events in East Antarctica: Impact on precipitation and their association with large-scale atmospheric circulation modes. *J. Clim.* **2024**, *37*, 1333–1345. [CrossRef]
21. Schlosser, E.; Manning, K.W.; Powers, J.G.; Duda, M.G.; Birnbaum, G.; Fujita, K. Characteristics of high-precipitation events in Dronning Maud Land, Antarctica. *J. Geophys. Res. Atmos.* **2010**, *115*, D14107. [CrossRef]
22. Maclennan, M.L.; Lenaerts, J.T.M. Large-scale atmospheric drivers of snowfall over Thwaites Glacier, Antarctica. *Geophys. Res. Lett.* **2021**, *48*, e2021GL093644. [CrossRef]
23. Birnbaum, G.; Brauner, R.; Ries, H. Synoptic situations causing high precipitation rates on the Antarctic plateau: Observations from Kohnen station, DML. *Antarct. Sci.* **2006**, *18*, 279–288. [CrossRef]
24. Yu, L.; Yang, Q.; Vihma, T.; Jagovkina, S.; Liu, J.; Sun, Q.; Li, Y. Features of extreme precipitation at Progress Station, Antarctica. *J. Clim.* **2018**, *31*, 9087–9105. [CrossRef]
25. Yang, R.; Yu, L.; Jagovkina, S.; Liang, K.; Yang, Q. Comparison of features of extreme precipitation between stations in inland and coastal Antarctica. *Int. J. Climatol.* **2023**, *43*, 996–1015. [CrossRef]
26. Schlosser, E.; Stenni, B.; Valt, M.; Cagnati, A.; Powers, J.G.; Manning, K.W.; Raphael, M.; Duda, M.G. Precipitation and synoptic regime in two extreme years 2009 and 2010 at Dome C, Antarctica-implications for ice core interpretation. *Atmos. Chem. Phys.* **2016**, *16*, 4757–4770. [CrossRef]
27. Marshall, G.J.; Thompson, D.W.J.; van den Broeke, M.R. The signature of Southern Hemisphere atmospheric circulation patterns in Antarctic precipitation. *Geophys. Res. Lett.* **2017**, *44*, 11580–11589. [CrossRef]
28. Zhu, Z.; Liu, J.; Song, M.; Hu, Y. Changes in extreme temperature and precipitation over the southern extratropical continents in response to Antarctic sea ice loss. *J. Clim.* **2023**, *36*, 4755–4775. [CrossRef]
29. Turner, J.; Lachlan-Cope, T.; Colwell, S.; Marshall, G.J. A positive trend in western Antarctic Peninsula precipitation over the last 50 years reflecting regional and Antarctic-wide atmospheric circulation changes. *Ann. Glaciol.* **2005**, *41*, 85–91. [CrossRef]
30. Rotschky, G.; Holmlund, P.; Isaksson, E.; Mulvaney, R.; Oerter, H.; van den Broeke, M.R.; Winther, J.-G. A new surface accumulation map for western Dronning Maud Land, Antarctica, from interpolation of point measurements. *J. Glaciol.* **2007**, *53*, 385–398. [CrossRef]
31. Thiery, W.; Gorodetskaya, I.V.; Bintanja, R.; van Lipzig, N.P.M.; van den Broeke, M.R.; Reijmer, C.H.; Munneke, P.K. Surface and snowdrift sublimation at Princess Elisabeth station, East Antarctica. *Cryosphere* **2012**, *6*, 841–857. [CrossRef]
32. Reijmer, C.H.; van den Broeke, M.R. Temporal and spatial variability of the surface mass balance in Dronning Maud Land, Antarctica, as derived from automatic weather stations. *J. Glaciol.* **2003**, *49*, 512–520. [CrossRef]
33. Noone, D.; Turner, J.; Mulvaney, R. Atmospheric signals and characteristics of accumulation in Dronning Maud Land, Antarctica. *J. Geophys. Res.* **1999**, *104*, 19191–19211. [CrossRef]

34. Lenaerts, J.T.M.; van Meijgaard, E.; van den Broeke, M.R.; Ligtenberg, S.R.M.; Horwath, M.; Isaksson, E. Recent snowfall anomalies in Dronning Maud Land, East Antarctica, in a historical and future climate perspective. *Geophys. Res. Lett.* **2013**, *40*, 2684–2688. [CrossRef]
35. Simon, S.; Turner, J.; Thamban, M.; Wille, J.D.; Deb, P. Spatiotemporal variability of extreme precipitation events and associated atmospheric processes over Dronning Maud Land, East Antarctica. *J. Geophys. Res.* **2024**, *129*, e2023JD038993. [CrossRef]
36. Yang, D.; Simonenko, A. Comparison of the results of measurements of winter precipitation by six Tretyakov sensors at the experimental site "Valdai". *Atmos. Ocean* **2013**, *52*, 39–53. [CrossRef]
37. Hersbach, H.; Bell, B.; Berrisford, P.; Hirahara, S.; Horányi, A.; Muñoz-Sabater, J.; Nicolas, J.; Peubey, C.; Radu, R.; Schepers, D.; et al. The ERA5 global reanalysis. *Q. J. R. Meteorol. Soc.* **2020**, *146*, 1999–2049. [CrossRef]
38. Gossart, A.; Helsen, S.; Lenaerts, J.T.M.; Broucke, S.V.; van Lipzig, N.P.M.; Souverijns, N. An evaluation of surface climatology in state-of-the-art reanalyze over the Antarctic ice sheet. *J. Clim.* **2019**, *32*, 6899–6915. [CrossRef]
39. Tetzner, D.; Thomas, E.; Allen, C. A validation of ERA5 reanalysis data in the southern Antarctic Peninsula—Ellsworth land region, and its implications for ice core studies. *Geosciences* **2019**, *9*, 289. [CrossRef]
40. Dong, X.; Wang, Y.; Hou, S.; Ding, M.; Yin, B.; Zhang, Y. Robustness of the recent global atmospheric reanalyses for Antarctic near-surface wind speed climatology. *J. Clim.* **2020**, *33*, 4027–4043. [CrossRef]
41. Caton Harrison, T.; Biri, S.; Bracegirdle, T.J.; King, J.C.; Kent, E.C.; Vignon, É.; Turner, J. Reanalysis representation of low-level winds in the Antarctic near-coastal region. *Weather Clim. Dyn.* **2022**, *3*, 1415–1437. [CrossRef]
42. Huang, B.; Thorne, P.W.; Banzon, V.F.; Boyer, T.; Zhang, H.-M. Extended reconstructed sea surface temperature version 5 (ERSSTv5), Upgrades, validations, and intercomparisons. *J. Clim.* **2017**, *28*, 911–930. [CrossRef]
43. Nan, S.L.; Li, J.P. The relationship between summer precipitation in the Yangtze River valley and the previous Southern Hemisphere Annular Mode. *Geophys. Res. Lett.* **2003**, *30*, 2266. [CrossRef]
44. Thompson, D.W.J.; Wallace, J.M. Annular modes in the extratropical circulation. Part I: Month-to-month variability. *J. Clim.* **2000**, *13*, 1000–1016. [CrossRef]
45. Mo, K.C.; Higgins, R.W. The Pacific–South American modes and tropical convection during the Southern Hemisphere winter. *Mon. Weather. Rev.* **1998**, *126*, 1581–1596. [CrossRef]
46. Ciasto, L.M.; Simpkins, G.R.; England, M.H. Teleconnections between tropical Pacific SST anomalies and extratropical Southern Hemisphere climate. *J. Clim.* **2015**, *28*, 56–65. [CrossRef]
47. Turner, J. The El Nino-southern oscillation and Antarctica. *Int. J. Climatol.* **2004**, *24*, 1–31. [CrossRef]
48. Yu, L.; Zhong, S.; Sui, C.; Zhang, Z.; Sun, B. Synoptic mode of Antarctic summer sea ice superimposed on interannual and decadal variability. *Adv. Clim. Change Res.* **2021**, *12*, 147–161. [CrossRef]
49. Zhang, C.; Li, T.; Li, S. Impacts of CP- and EP-EL Nino events on the Antarctic sea ice austral spring. *J. Clim.* **2021**, *34*, 9327–9348. [CrossRef]
50. Liang, K.; Wang, J.; Luo, H.; Yang, Q. The role of atmospheric rivers in Antarctic sea ice variations. *Geophys. Res. Lett.* **2023**, *50*, e2022GL102588. [CrossRef]
51. Yu, L.; Zhong, S.; Vihma, T.; Sui, C.; Sun, B. Multidecadal variations in North Atlantic SSTs modulate the relationship between ENSO and the South Atlantic Subtropical Dipole since 1900. *Environ. Res. Lett.* **2024**, *19*, 094001. [CrossRef]
52. Yu, L.; Zhong, S.; Vihma, T.; Sui, C.; Sun, B. Enhanced interaction between ENSO and the South Atlantic Subtropical Dipole over the past four decades. *Int. J. Climatol.* **2024**, *44*, 4192–4205. [CrossRef]